# Modeling the interaction of microbubbles: Effects of proximity, confinement, and excitation amplitude

W. Wiedemair, Z. Tukovic, H. Jasak, D. Poulikakos, and V. Kurtcuoglu

Citation: Physics of Fluids (1994-present) **26**, 062106 (2014); doi: 10.1063/1.4883482
View online: http://dx.doi.org/10.1063/1.4883482
View Table of Contents: http://scitation.aip.org/content/aip/journal/pof2/26/6?ver=pdfcov
Published by the AIP Publishing

PHYSICS OF FLUIDS **26**, 062106 (2014)

# Modeling the interaction of microbubbles: Effects of proximity, confinement, and excitation amplitude

W. Wiedemair,[1] Z. Tukovic,[2] H. Jasak,[2] D. Poulikakos,[1,a)]
and V. Kurtcuoglu[3,a)]
[1]*Laboratory of Thermodynamics in Emerging Technologies, Department of Mechanical and Process Engineering, ETH Zurich, Sonneggstrasse 3, 8092 Zurich, Switzerland*
[2]*Faculty of Mechanical Engineering and Naval Architecture, University of Zagreb, Ivana Lucica 5, 10000 Zagreb, Croatia*
[3]*The Interface Group, Institute of Physiology, University of Zurich, Winterthurerstrasse 190, 8057 Zurich, Switzerland*

(Received 9 September 2013; accepted 3 June 2014; published online 20 June 2014)

The interaction of closely spaced microbubbles (MBs) exposed to a transient external pressure field is relevant for a variety of industrial and medical applications. We present a computational framework employing an interface tracking approach to model the transient dynamics of multiple, interacting, insonated MBs in arbitrary settings. In particular, this technique allows studying the effects of mutual proximity, confinement, and variations in excitation amplitude on the translatory motion of pairs of differently sized MBs. Domains of mutual repulsion or attraction are observed for closely spaced MBs in the investigated range of excitation frequencies. The repulsion domain widens and shifts to lower frequencies with increasing excitation pressure amplitude. When the MBs are confined in rigid tubes of decreasing diameters, we observe a shift of the translatory patterns towards lower frequencies, accompanied by a change in relative strength of the two translation modes. This effect is correlated to a decrease of the resonance frequency due to confinement which causes changes in oscillation amplitude and phase shift between the bubble vibrations. Coupling to the viscous host liquid gives rise to phenomena such as collective MB drift, non-symmetric attraction or repulsion, and reversal of translation direction. A system comprising six MBs inside a narrow tube highlights the potential of the computational framework to treat complex setups with multiple bubbles. © *2014 AIP Publishing LLC*. [http://dx.doi.org/10.1063/1.4883482]

## I. INTRODUCTION

A growing range of ultrasound (US) applications relies on gas-filled microbubbles (MBs) as agents to create or augment a desired effect. The spectrum comprises technological applications such as the cleaning of surfaces,[1] especially of wafers in microelectronics processing[2] and of optical devices, as well as medical use for surgical instrument disinfection[3] or removal of biofilms.[4] In medicine, MBs have been employed for decades as contrast agent for diagnostic US.[5] More recently, they have been utilized for targeted drug delivery[6] and the transient opening of the blood-brain barrier.[7–9] In all these applications, an ensemble of MBs is exposed to US and the desired response is generated by the coupled dynamics of the MBs. Yet, the processes driving these applications are insufficiently understood. The capability to model the interaction of MBs in configurations relevant for the above applications would grant insight into the involved dynamics, which could then be used for process optimization. This study is specifically geared towards the excitation parameter range, microbubble size, and configurations relevant for medical applications.

[a)]Authors to whom correspondence should be addressed. Electronic addresses: dpoulikakos@ethz.ch and vartan.kurtcuoglu@uzh.ch

 

The response of individual MBs in an infinite liquid volume to an incident US field has been studied extensively[10] and is analytically described.[11] Moreover, some aspects of MB dynamics in a confined space can be predicted.[12] The non-linear response of MBs to increasing levels of ultrasound excitation was examined by Lauterborn[13] employing frequency response curves. In the last decade experimental investigations[14] have profited from the availability of ultra-high frame rate cameras.[15] However, capturing the small length scales and the rapid vibrations of MBs in the MHz frequency range remains challenging, especially when multiple bubbles are considered.

The force resulting from a spatial pressure gradient acting on a vibrating bubble was investigated by Bjerknes.[16] This gradient may either be created by an external source, giving rise to the primary Bjerknes force ($\mathbf{f}_{B1}$), or caused locally by the vibrations of a neighboring bubble, resulting in the secondary Bjerknes force ($\mathbf{f}_{B2}$). The interaction of two MBs is governed by the latter force, which, according to linear theory, determines mutual attraction or repulsion depending on the difference in vibration phase.[17] For simplified systems where the MBs retain a spherical shape throughout the oscillation cycle and are spaced sufficiently far apart, the dynamics can be studied by analytical means.[18,19] Most derivations assume viscous, incompressible host liquids, and adiabatically compressible bubbles.[20–22] Non-spherical oscillations of MBs in close proximity in an inviscid, incompressible liquid were studied by Pelekasis and Tsamopoulos[23] using Legendre modes. The influence of non-linear pulsations on the translation direction was investigated by Oguz and Prosperetti[19] using a virial theorem approach which was further developed and refined by Harkin *et al.*[24] Doinikov[25] proposed a model for the time-averaged dynamics of multiple bubbles spaced at arbitrary distances and specifically addresses the time-averaged force of closely spaced air bubbles in an inviscid fluid.[26] The direction of this force depends also on the distance between the MBs[22] and the excitation amplitude.[18] A detailed review of the topic is provided by Doinikov.[27]

Experimental observations of $\mathbf{f}_{B2}$ are reported by Garbin *et al.*,[28] who studied the impact of close-by walls or neighboring MBs on the oscillation pattern of an MB. Marmottant *et al.*[29] investigated the oscillatory and translator dynamics of a MB interacting with a wall using ultra-fast imaging technologies.[15] Yoshida *et al.*[30] reported the observation of changes in direction of the relative motion of two MBs and its dependence on their distance. The aggregation of stable bubble clusters,[31] called bubble grapes, could be related to this phenomenon.[32]

Volume of fluid,[33] level set,[34] and front tracking[35,36] methods have been proposed to describe the bubble interface, for example, in the modeling of rising macroscopic gas bubbles.[37–41] An interface tracking algorithm employing marker particles on a static grid[42] was employed by Ye and Bull[43] to model the expansion of a bubble inside a flexible tube. Hosseinkhah and Hynynen[44] addressed ultrasound induced oscillations of individual microbubbles in a viscous incompressible fluid inside compliant microvessels, while the dynamics of a single bubble near a rigid wall in an inviscid host liquid was investigated by Zhang *et al.*[45] using boundary integrals. Hsiao and Chahine[46] used a boundary element approach to model the non-spherical dynamics of encapsulated microbubbles for medical purposes. Mendez and Gonzalez-Cinca[47] employed a similar modality to model the interaction of insonated bubble pairs in an inviscid, incompressible fluid. The interaction of multiple bubbles was simulated by Kawamura and Kodama[48] in turbulent flow conditions using a front tracking algorithm.

Current theoretical models for MB interaction are limited in their generality by assuming either widely separated spherical bubbles, inviscid host liquids, or by resorting to averaged dynamics without a full consideration of the physics of the surrounding liquid dynamics. Experimental observations require large efforts to allow insight into kinematics, but lack the ability to assess important dynamic properties like pressure. We have developed a computational framework (CF) that is capable of modeling the transient interaction of multiple, arbitrarily positioned MBs in an incompressible, viscous, isothermal, Newtonian liquid excited by a transient pressure field. This framework enables the study of configurations that are not readily accessible to theoretical models or experimental techniques, and allows for the harvesting of a wealth of important kinematic and dynamic information. Here we focus on assessing the influence of bubble spacing, excitation pressure, and confinement on MB dynamics, studying in particular the uniaxial translatory behavior along the MB conjugation line. The geometric setups and parameter ranges are chosen to be of relevance for intravascular microbubble dynamics in medical applications.

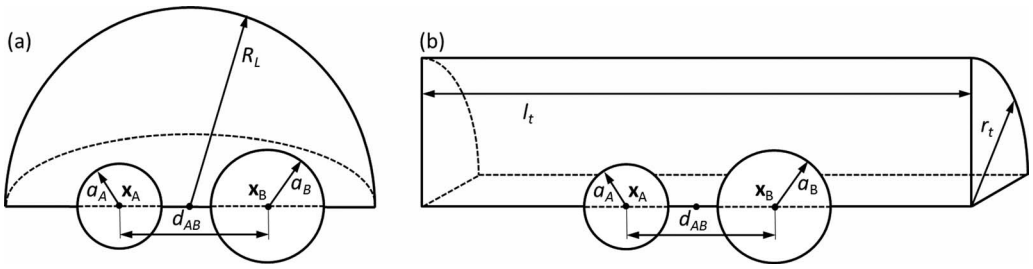


FIG. 1. Setups used to study the interaction of two MBs in a large liquid envelop (a) and inside a cylindrical tube (b). $a_A$ and $a_B$ denote the MB radii, $\mathbf{x}_A$ and $\mathbf{x}_B$ are the positions of the MB centers, and $d_{AB}$ is the distance between these centers. Drawings are not to scale.

## II. MATERIALS AND METHODS

Two different sets of axisymmetric geometries are considered, where MBs are immersed in an incompressible, viscous liquid either arranged along a common axis inside a very large sphere of radius $R_L$, mimicking an infinite liquid envelop as assumed in many theoretical treatments, or situated along the axis of a rigid cylindrical tube of variable radius $r_t$ (Figure 1). These setups enable the study of the effects of MB proximity, varying excitation amplitude, and of spatial confinement on MB dynamics and kinematics.

A numerical solver tailored to address this problem setting was developed in the OpenFOAM numerical platform.[49] The solver relies on an interface tracking approach,[50] where the gas-liquid interface coincides with a boundary of the mesh and hosts an adaptable boundary condition that is updated according to the conditions in the MB. This gas-liquid boundary is deformed until force equilibrium,

$$P_i = P_g - \sigma\kappa - 2\mu\nabla_S \cdot \mathbf{v}_\mathrm{i}, \tag{1}$$

is reached at the interface. Here, $P_i$ is the liquid pressure at the interface, $\sigma$ is the surface tension, $\mu$ is the dynamic viscosity of the liquid, and $\mathbf{v}_\mathrm{i}$ denotes the liquid velocity at the interface. The letter $\kappa$ denotes twice the local curvature of the interface calculated by $\kappa = -\nabla_s \cdot \tilde{\mathbf{n}}$, where $\nabla_\mathrm{s}$ is the surface gradient operator defined as $\nabla_\mathrm{s} = \nabla - \tilde{\mathbf{n}}\tilde{\mathbf{n}} \cdot \nabla$ with $\tilde{\mathbf{n}}$ being the interface unit normal vector pointing out of the liquid domain. $P_g$ is the pressure inside the MB, considered homogeneous and only dependent on time. It is calculated via a polytropic law

$$P_g = P_{g,0}\left(\frac{V_{b,0}}{V_b}\right)^{\gamma}, \tag{2}$$

where $P_{g,0}$ is the equilibrium gas pressure, $V_{b,0}$ is the MB equilibrium volume, $V_b$ is the current MB volume, and $\gamma$ is the polytropic exponent. This simplification is applicable because the wavelength in the gas is considerable larger than the size of the MB[11] such that no mayor pressure gradients may establish inside a MB: Considering a bubble of 2 $\mu$m diameter and speed of sound in air of 343 m/s,[51] the maximum attainable pressure gradient is 1.8% of the peak-to-peak pressure amplitude. This introduces a maximum uncertainty of $<1.2\%$ in the MB radius, translating to a similar uncertainty in $\kappa$ and in the viscous stress term in Eq. (1). Due to the local determination of $\kappa$, $P_i$, and $\mathbf{v}_\mathrm{i}$, Eq. (1) is able to handle non-linear bubble vibrations leading to non-spherical shapes. $V_b$ and the position of the center of gravity $\mathbf{x}_\mathrm{b}$ of the MB are determined from the vertex positions on the interface mesh. The index $b$ in the equations is a placeholder for the letter designating a specific MB, introduced later in the text.

The liquid domain is resolved with an unstructured hexahedral mesh covering a quarter of the actual rotationally symmetric geometry and symmetry boundary conditions are used to account for the entire domain. This mesh is deformed to accommodate the motion of the bubble interface using a vertex-based dynamic mesh adaptation method[52] that employs Laplace point diffusion in conjunction with tetrahedral cell decomposition. This algorithm is capable of accommodating severe deformations while maintaining a valid, high quality mesh. Computation is terminated if the criteria

for solution convergence are no longer met or the continuously monitored quality of the deformed mesh falls below pre-set thresholds, which is particularly relevant for the close approach of two MBs and the related distortion of the interjacent cells. This procedure, while computationally costly, allows retaining the sharp bubble-liquid interface throughout the computation. A precisely defined, smooth interface is indispensable for an exact determination of $\kappa$, which is needed to accurately evaluate Eq. (1) that is dominated by the surface tension term due to large MB curvature.

The flow of an incompressible, viscous fluid in an arbitrarily shaped volume $V$ bounded by a moving surface $S$ is governed by the conservation laws for mass and linear momentum:

$$\int_S \mathbf{n} \cdot \mathbf{v} \, \mathrm{d}S = 0, \tag{3}$$

$$\frac{\mathrm{d}}{\mathrm{d}t} \int_V \mathbf{v} \, \mathrm{d}V + \int_S \mathbf{n} \cdot (\mathbf{v} - \mathbf{v}_s) \mathbf{v} \, \mathrm{d}S = \int_S \mathbf{n} \cdot (\nu \nabla \mathbf{v}) \, \mathrm{d}S - \frac{1}{\rho} \int_V \nabla P \, \mathrm{d}V, \tag{4}$$

where $\mathbf{v}$ denotes the liquid velocity, $\mathbf{v}_s$ is the displacement velocity of the surface $S$, $\mathbf{n}$ is the outward pointing unit normal on $S$, $\rho$ denotes liquid density, $\nu = \mu \cdot \rho^{-1}$ is the kinematic viscosity of the liquid, and $P$ is the pressure. The space conservation law[53] defines the relationship between the rate of change of the volume $V$ and $\mathbf{v}_s$ :

$$\frac{\mathrm{d}}{\mathrm{d}t} \int_V \mathrm{d}V - \int_S \mathbf{n} \cdot \mathbf{v_s} \, \mathrm{d}S = 0. \tag{5}$$

These governing equations are applicable to a dynamically deforming computational mesh and use an arbitrary Lagrangian-Eulerian (ALE) formulation. The equations are discretized in space using a second order accurate finite volume method (FVM) formulation for a collocated, cell-centered field variable arrangement on an unstructured 3D mesh. The algebraic model consists of a discretized momentum equation and a discretized pressure equation, which is obtained by combining the momentum and continuity equations using the Rhie-Chow momentum interpolation method.[54] Discretization employs a bounded linear deferred correction scheme with skewness correction for the convection term and a central difference scheme with non-orthogonality correction for the Laplacian terms. The transient problem is treated in a time-marching manner with uniform time steps $\Delta t$. An implicit second order accurate three-time-level scheme[55] is employed for the temporal discretization. The resulting algebraic system is solved in a segregated pressure-velocity coupling procedure based on the PISO algorithm[56] using preconditioned conjugate and bi-conjugate gradient schemes for the pressure and momentum equations, respectively.

Water was taken as the liquid to host the MBs, setting dynamic viscosity to $\mu = 10^{-3}$ kg m$^{-1}$ s$^{-1}$ and density to $\rho = 1000$ kg m$^{-3}$. Compressibility of the liquid is neglected for the examined range of frequencies[57] and small pressure amplitudes[18,38] because radiation damping is much smaller than viscous damping[38] for low acoustic Mach numbers. We verified this assumption by comparing the results yielded by the incompressible Rayleigh-Plesset model[11] with the Keller-Miksis model[10] (see Appendix B). Attenuation or absorption was not considered in this model because the small absorption coefficient $\alpha = 0.0022$ dB/cm/MHz[58] of the liquid causes a negligible pressure amplitude drop (<0.002%) even for the highest employed frequencies in domains of the sizes considered here. In view of medical applications, also surrounding tissues ($\alpha = 0.54$ dB/cm/MHz) or whole blood (0.2 dB/cm/MHz)[58] cause a very limited amplitude drop of 0.1% of a 1 MHz signal in a 100 $\mu$m domain. The gas inside the MBs is considered to have properties similar to air, rendering $\sigma = 0.07323$ kg s$^{-2}$, while the density and viscosity of the gas are negligible. Adiabatic compression and expansion are assumed, yielding $\gamma = 1.4$.

A transient sinusoidal pressure, varying around a pressure baseline level of $P_0 = 0$ Pa, is applied at the outer boundary of the liquid envelop or the inlets of the tube, respectively. The considered frequency $f_{ex}$ of this external excitation ranges from 100 kHz to 5 MHz with pressure amplitudes $P_{ex}$ between 10 kPa and 50 kPa. With a speed of sound in water of $c_w = 1480$ m/s,[58] the wavelength in the relevant frequency range is $\lambda_w = 0.3$–15 mm, which is much larger than the diameter of a MBs

or the distance between the MBs. The maximum spatial pressure gradient $2 \cdot \pi \cdot P_{ex}/\lambda_w$ imposed by the external field at the highest $f_{ex}$ could cause a pressure variation across the MB diameter of less than 0.5% of the peak-to-peak pressure amplitude of the external field. Therefore, $\mathbf{f}_{\mathrm{B1}}$ can be neglected and $P_{ex}$ is assumed to vary synchronously at all domain boundaries.

This modelling approach inherently assumes transmissive boundaries and neglects any change in pressure patterns due to reflections at those. This is a reasonable assumption for medical intravascular applications given the close match of the acoustic impedances of the liquid phase and tissue;[58] the resulting reflection coefficient for normal incidence is below 2% at their interface. The MB vibrations are incited by this external pressure stimulus which acts on the interface between the incompressible liquid and the compressible MB gas content, causing the MB to change volume according to Eq. (2) in order to meet the dynamic equilibrium required by Eq. (1).

Prior to the actual study, the numerical solver was examined in detail with respect to its numerical stability and consistency (see Appendixes A and B). Discretization independence studies confirm that the results reported herein are grid and time step size independent. The validity of the results is confirmed by comparison of the numerical results with analytical predictions for bubble oscillation and bubble translation.

## III. RESULTS

We examine the interaction of MBs of equilibrium radius $a_{0,A} = 1\ \mu$m (bubble A) and $a_{0,B} = 1.2\ \mu$m (bubble B), relevant for medical applications, in different setups. Starting from a situation where a pair of MBs of different size is spaced far apart inside a large liquid envelope, we investigate the impact of excitation amplitude variations and the effect of moving the MBs closer together. Subsequently, the closely spaced configuration is confined inside rigid tubes of different diameters, and finally the number of MBs is increased. MBs of that size[59,60] with an added encapsulating layer are commonly used in medical applications[6] in the selected frequency range.[61] Confining tube sizes are chosen according to blood vessel dimensions on the capillary[62] and pre-capillary levels.

### A. Excitation pressure dependence

Most analytical studies consider bubbles in an unbounded space, separated by a distance $d_{bb}$ substantially larger than their diameters. Here we start similarly, to facilitate comparisons, by studying the response of a MB pair with initial $d_{bb} = 40\ \mu$m (setup I) inside a large spherical liquid envelope of radius $R_L = 100\ \mu$m. This configuration is exposed to a sinusoidal driving pressure at three different amplitudes settings of 10 kPa, 30 kPa, and 50 kPa with $f_{ex}$ ranging from 1 MHz to 5 MHz.

The oscillation range $\Delta\bar{a}$ of the MB vibration is found by drawing a signal envelope over the transient, spatially averaged radius $\bar{a}$ of each bubble and comparing the instantaneous maximum and minimum values at an instance when most oscillations have reached a steady amplitude level. The plot of this parameter over a certain frequency range yields the frequency response curve and is an indicator for the resonance properties of a MB.[13] The frequency response curves of the MBs in setup I for the three $P_{ex}$ setting are displayed in Figure 2. At low $P_{ex}$, the $\Delta\bar{a}$ pattern of each MB shows a single maximum response peak of height $\Delta\bar{a}_{max}$ at a maximum response frequency $f_{\Delta\bar{a},max}$ of 3.4 MHz for bubble A and 2.6 MHz for bubble B.

The linear resonance frequency of a single MB in an infinitely large, viscous fluid envelope can be calculated as

$$f_r = \sqrt{\frac{1}{4\pi^2\rho a_0^2}\left(3\gamma P_0 + \frac{2\sigma}{a_0}(3\gamma - 1)\right) - \frac{4\mu^2}{2\pi^2 a_0^4 \rho^2}}, \tag{6}$$

where the last term on the right hand side accounts for viscous damping.[63] Resonance frequencies of $f_{r,A} = 3.394$ MHz for a MB of $a_{0,A} = 1\ \mu$m and $f_{r,B} = 2.586$ MHz for a MB of $a_{0,B} = 1.2\ \mu$m are predicted by this formula, which is in excellent agreement with the low amplitude numerical results.

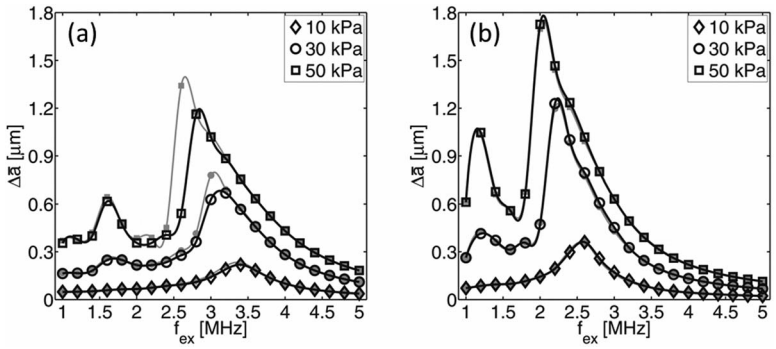


FIG. 2. Frequency dependent $\Delta\bar{a}$ response for two interacting MBs of $a_{0,A} = 1$ $\mu$m (a) and $a_{0,B} = 1.2$ $\mu$m (b) with $d_{bb} = 40$ $\mu$m (setup I) at $P_{ex}$ levels of 10 kPa, 30 kPa, and 50 kPa. The increase in excitation pressure causes a growth of $\Delta\bar{a}_{max}$ and a shift of $f_{\Delta\bar{a},max}$ to lower $f_{ex}$ values from 3.4 MHz via 3.1 MHz to 2.8 MHz for bubble A and from 2.6 MHz via 2.2 MHz to 2.0 MHz for bubble B. The low frequency slope of the main peaks steepens and secondary peaks establish at lower $f_{ex}$. The acquired results are underlaid with the theoretical predictions (grey) for single MBs from the RPE. Numerical and analytical results show excellent agreement for bubble B and an offset in $\Delta\bar{a}_{max}$ and $f_{\Delta\bar{a},max}$ for bubble A at higher $P_{ex}$ values.

With increasing $P_{ex}$ the maximum response $\Delta\bar{a}_{max}$ grows and $f_{\Delta\bar{a},max}$ shifts to lower values of $f_{ex}$, passing from 3.4 MHz to 2.8 MHz for bubble A and from 2.6 MHz to 2.0 MHz for bubble B. The low frequency slope of the main peak steepens markedly with growing $P_{ex}$ and secondary peaks appear close to half the maximum response frequencies. These results are compared to $\Delta a$ predictions by the Rayleigh-Plesset equation (RPE, see Appendixes A and B) for single spherical MBs at similar settings (grey lines in Figure 2). We observe a close correspondence for the larger bubble and a slight offset in peak position and height for the smaller bubble.

### B. Bubble proximity

The secondary Bjerknes force $\mathbf{f}_{B2}$ scales inversely with the square of the distance $d_{bb}$ between bubbles. Marked differences in coupled MB dynamics can thus be expected when decreasing $d_{bb}$ to 6 $\mu$m (setup II). A comparison between the vibrations of the MBs in setups I and II exposed to a sinusoidal driving pressure of $P_{ex} = 50$ kPa at $f_{ex} = 2.8$ MHz is depicted in Figure 3. The vibration amplitude of the smaller MB is strongly reduced when the two MBs approach. Moreover, their previously rather phase synchronous vibrations acquire a phase offset.

The $\Delta\bar{a}$ response of the closely spaced configuration for $f_{ex}$ ranging from 1 MHz to 5 MHz at the three $P_{ex}$ levels is depicted in Figure 4. Similar to setup I, the peaks in $\Delta\bar{a}$ grow and shift towards lower frequencies with growing $P_{ex}$. The pattern of the larger bubble B remains almost unaltered by the decrease in $d_{bb}$ in the monitored frequency range. On the other hand, bubble A exhibits a

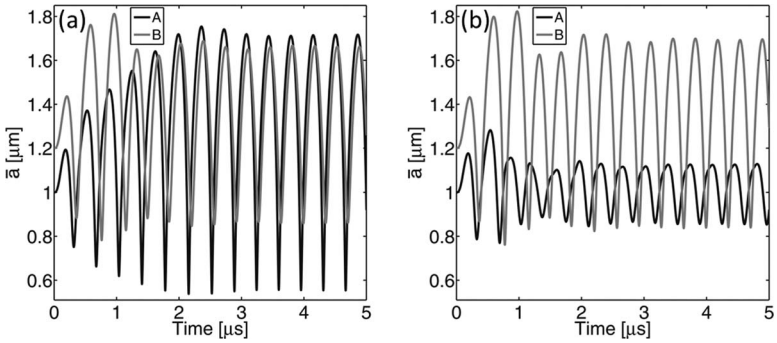


FIG. 3. Radius-time curves of the MB pair when separated by 40 $\mu$m (a) and 6 $\mu$m (b) and exposed to a transient pressure of $P_{ex} = 50$ kPa and $f_{ex} = 2.8$ MHz. While bubble B retains its pattern and amplitude almost unchanged, bubble A suffers a major decrease in amplitude and also acquires a larger phase shift with respect to bubble B.

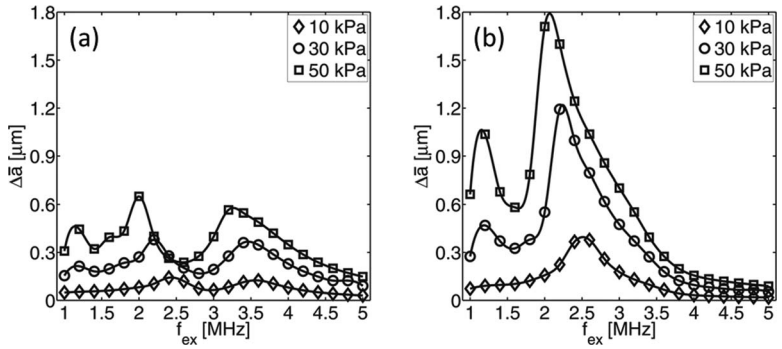


FIG. 4. Frequency response curves for $d_{bb} = 6\ \mu$m at three $P_{ex}$ settings. (a) Bubble A exposes two peaks of almost equivalent height. The low frequency peak aligns with the main peak of bubble B and the high frequency one is shifted to higher $f_{ex}$ values compared to setup I. For both MBs, $\Delta\bar{a}_{max}$ grows and $f_{\Delta\bar{a},max}$ decreases with increasing values of $P_{ex}$. (b) The response of the larger bubble B shows no appreciable changes compared to setup I.

low frequency peak that is aligned with the main peak of bubble B, even in the linear $P_{ex}$ regime. Its high frequency peak is considerably diminished as compared to setup I and shifted to higher frequencies of 3.6 MHz, 3.4 MHz, and 3.2 MHz at the respective $P_{ex}$ levels of 10 kPa, 30 kPa, and 50 kPa, respectively. The frequency gap of 1.2 MHz between the two peaks appears to remain constant during the shifts. Due to the inhomogeneous pressure field at their interfaces caused by the proximity of the neighbor, the MBs oscillate not only in volume but also in shape. The deviation from the spherical shape measured by

$$\beta = \frac{a_{\max} - a_{\min}}{a_{\max}} \tag{7}$$

increases with decreasing distance between the MBs. Here $a_{max}$ and $a_{min}$ are, respectively, the maximum and minimum distances of a surface element from the center of gravity of the MB at a given instant. At the applied low pressure amplitudes, the MBs stay almost spherical ($\beta < 0.05$) for more than 90% of the oscillation cycle, with peak $\beta$ values not exceeding 0.22. In configurations with low $\Delta\bar{a}$, $\beta$ remains below 0.01 for the entire duration of excitation. The bubble surface stays smooth during the simulation without the formation of surface ripples.

In addition to their individual vibrations, the MBs respond to a transient external pressure by a translation relative to each other. Attraction between the MBs is signaled by a negative value of their average relative velocity, $v_{bb} = \langle \mathrm{d}(d_{bb})/\mathrm{d}t \rangle$, measured along the bubbles' center-to-center axis (CCA), while repulsion acquires a positive sign. The frequency dependence of $v_{bb}$ (Figure 5, top row) shows two domains of attraction framing a domain of repulsion. The average phase offset $\theta$ between the oscillation patterns of bubble A and bubble B (Figure 5, center row) is determined by the relative temporal distance of their well-defined radius minima. Bubble repulsion is correlated with phase offsets of approximately 90° or higher.

The assessment of $v_{bb}$ and $\theta$ is performed for three $P_{ex}$ values of 10 kPa, 30 kPa, and 50 kPa. The repulsive region widens and shifts to lower frequencies with increasing $P_{ex}$, thereby displacing the transitions between attraction and repulsion from 3.1 MHz and 3.5 MHz to 2.3 MHz and 3.3 MHz, respectively. The peak values of $v_{bb}$ grow with $\Delta\bar{a}_{max}$, which increases with $P_{ex}$. The low frequency attractive $v_{bb}$ peak appears in the vicinity of the common $f_{\Delta\bar{a},max}$ of the two bubbles.

In addition to considerations on frequency dependent average translation, the investigation of the transient behavior of MB pairs at selected $f_{ex}$ reveals further interesting phenomena. To visualize them, a technique similar to streak images[64] used in experimental MB observation is employed. It captures the portions of CCA covered by a MB at every time instance and encodes the normal distance of the MB surface from the axis by brightness shading. This allows for display of oscillation and translational in one graph while the superimposed lines trace the position of the MB centers.

A selection of streak plots acquired from setup II at $P_{ex} = 50$ kPa and different excitation frequencies shows that the small MB tends to move faster towards the larger MB upon attraction,

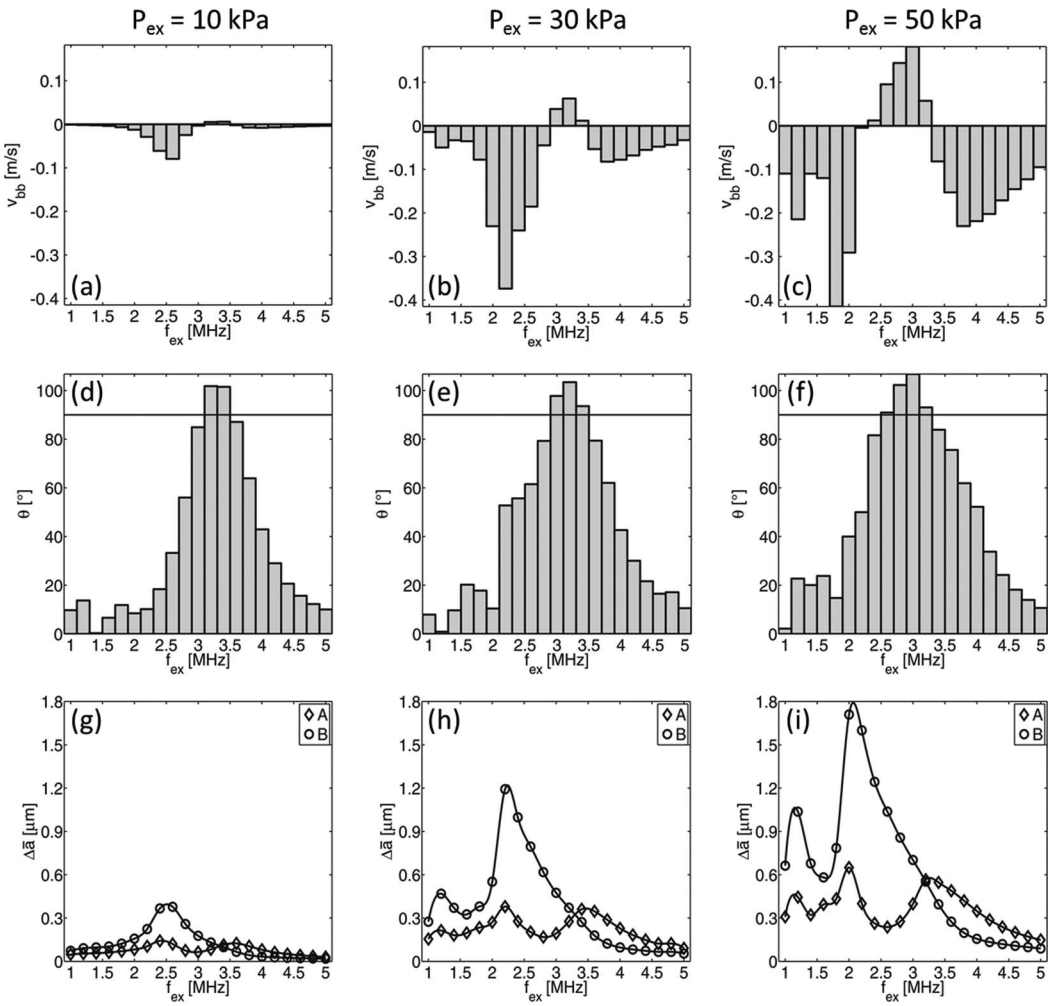


FIG. 5. Frequency dependence of $v_{bb}$ (a)–(c), $\theta$ (d)–(f), and $\Delta\bar{a}$ (g)–(i) for $P_{ex} = 10$ kPa (a), (d), (g); $P_{ex} = 30$ kPa (b), (e), (h); and $P_{ex} = 50$ kPa (c), (f), (i) in setup II. The relative velocity shows a transition between attraction at low $f_{ex}$ to repulsion in the range where $\theta$ is roughly at or above 90°, and attraction again at higher frequencies. Increasing $P_{ex}$ levels cause a widening of the repulsion region, its shift towards lower frequencies, and a rise in peak relative velocities. The strongest attraction is observed in the vicinity of the common $f_{\Delta\bar{a},max}$ of the two bubbles.

but the larger MB shows much stronger drift away from the common center in case of repulsion (Figure 6). The bubbles may also drift in the same direction at different speeds. Finally, the direction of motion can change when the MBs have reached a certain distance from each other.

In a perfectly symmetric configuration comprising two MBs of $a_0 = 1.2$ $\mu$m spaced with $d_{bb} = 6$ $\mu$m in a liquid sphere of $R_L = 100$ $\mu$m (setup IIa), the MBs attract each other at all inspected $f_{ex}$ settings in a perfectly symmetric way. The computation stops when the mesh between the MB surfaces is compressed by approximately a factor of 25, as this causes deterioration of the mesh quality below the pre-set thresholds. Two sample streak plots of MBs inside a large liquid envelope exposed to $P_{ex} = 50$ kPa are shown in Figure 7. The MBs approach each other considerably faster when excited at $f_{ex} = 2.8$ MHz than at $f_{ex} = 3.2$ MHz.

### C. Impact of confinement

The influence of bubble confinement is investigated using three setups of rigid circular cylindrical tubes of different radii $r_t$, MB spacing of 6 $\mu$m and $P_{ex} = 40$ kPa: $r_t = 20$ $\mu$m (setup III), $r_t = 7.5$ $\mu$m (setup IV), and $r_t = 3$ $\mu$m (setup V). Such tubes correspond in terms of geometry to idealized

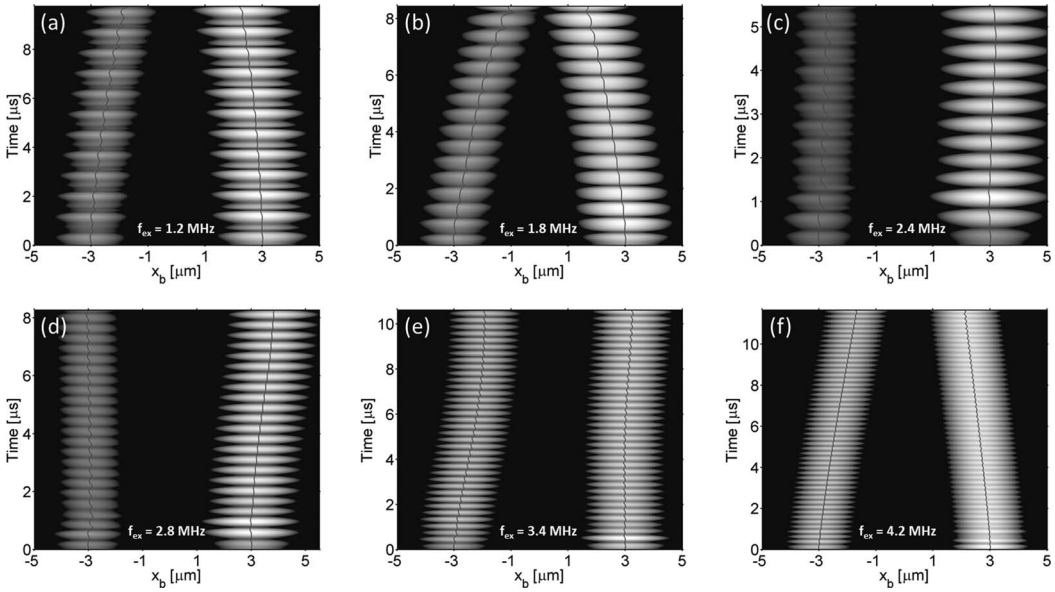


FIG. 6. Selected streak plots of two oscillating MBs at $d_{bb} = 6\ \mu$m and $P_{ex} = 50$ kPa inside a large liquid envelope (setup II). At $f_{ex} = 1.2$ MHz (a) and $f_{ex} = 1.8$ MHz (b) the smaller MB is attracted at higher speed than its counterpart. At 2.4 MHz (c) the MBs remain approximately in place while at 2.8 MHz (d), the larger MB drifts away from the common center and the small MB stays almost in place. This pattern develops at 3.4 MHz (e) into a situation where the smaller MB is initially drawn towards a rather static larger MB, which then starts to move out while the smaller MB slows down its approach, leading to a switch from overall attraction to repulsion. At 4.2 MHz (f), the MBs attract each other again with the small MB being drawn in faster than the large one.

capillary[62] and pre-capillary[65] blood vessels. We assess the frequency dependence of $v_{bb}$, $\Delta\bar{a}$, and $\theta$ for these configurations. The domain of repulsion moves towards lower frequencies when the tube narrows (Figure 8). At the same time, the speed of repulsion and high frequency attraction decreases, while the attraction at lower frequencies gains in relative magnitude with its peak shifting from 1.9 MHz via 1.7 MHz to 0.7 MHz. The two frequencies of transition between repulsion and attraction correspond closely to the $f_{ex}$ values where $\theta$ crosses 90°. It is remarkable that lower local peaks in $\theta$ occur at fractions of the central frequency of repulsion. This behavior is particularly prominent in the narrowest tube. A gradual decrease of $f_{\Delta\bar{a},max}$ for both MBs from 1.6 MHz to 1.4 MHz and finally to 0.7 MHz, as well as a diminishing high frequency peak for bubble A are observed. The $\Delta\bar{a}$ patterns of both bubbles become more similar in shape with decreasing $r_t$, and $\Delta\bar{a}_{max}$ decreases for both MBs.

The asymmetries in translation of the MBs, identified above for setup II (Figure 6), are also observed in confinement. However, the features appear less pronounced as can be assessed from a comparison of the trace of the MB centers (Figure 9). These traces show a transition of MBs

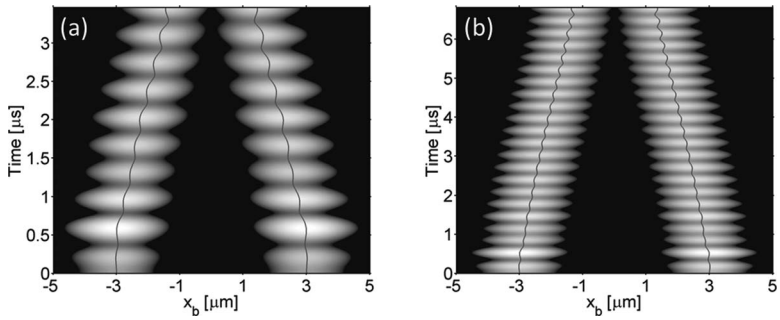


FIG. 7. Streak plots of two identical MBs of $a_0 = 1.2\ \mu$m at $d_{bb} = 6\ \mu$m exposed to a transient pressure of $P_{ex} = 50$ kPa. The MBs approach each other at about double the speed for $f_{ex} = 2.8$ MHz (a) compared to $f_{ex} = 3.2$ MHz (b).

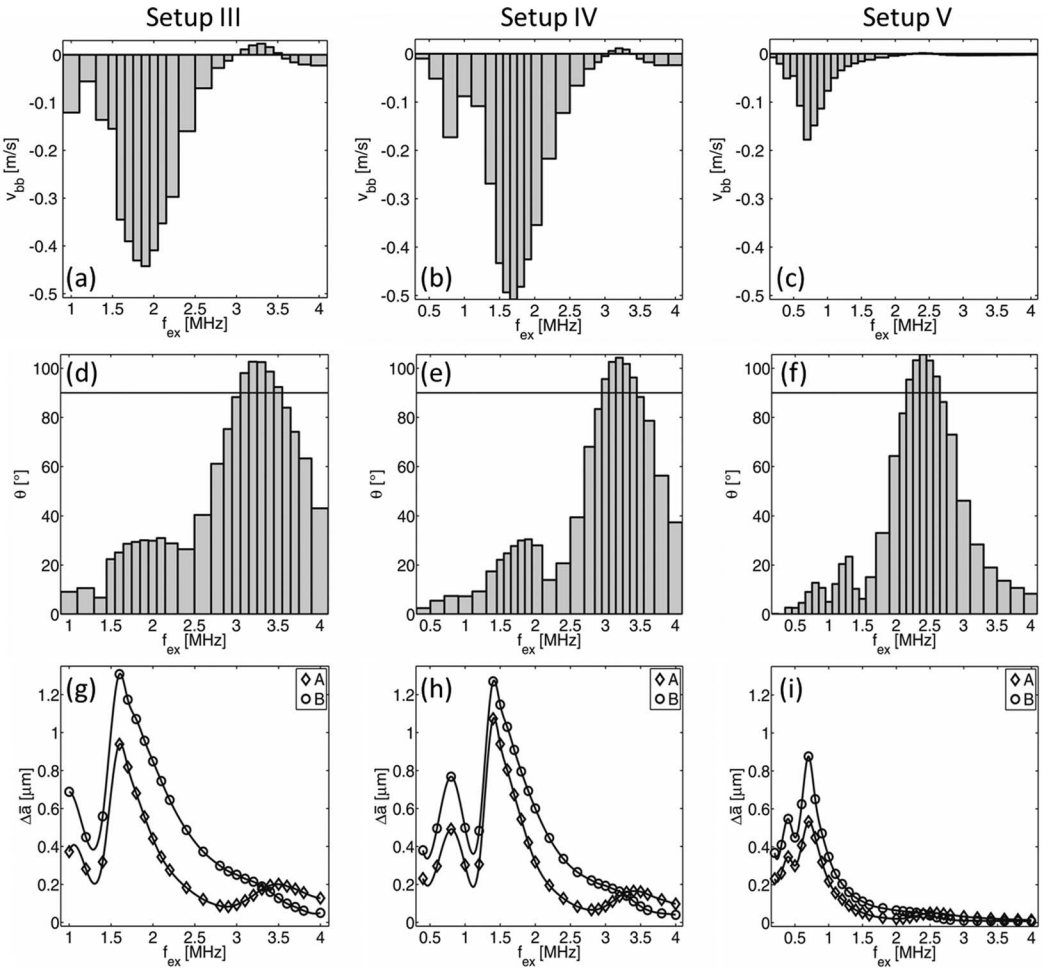


FIG. 8. Comparison of the frequency dependent characteristics of pairs of MBs with $a_{0,A} = 1\ \mu$m and $a_{0,B} = 1.2\ \mu$m exposed to a transient pressure field of $P_{ex} = 40$ kPa inside a rigid tube of $r_t = 20\ \mu$m (a), (d), (g); $r_t = 7.5\ \mu$m (b), (e), (h); and $r_t = 3\ \mu$m (c), (f), (i). (a)–(c) With decreasing $r_t$, the repulsive region diminishes in strength relative to the attractive region and both shift towards smaller $f_{ex}$. (d)–(f) $\theta$ crossing 90° reflects very accurately the transition between repulsion and attraction. Secondary and even tertiary peaks in $\theta$ establish with decreasing $r_t$. (g)–(i) Reduction of $r_t$ results in a shift of the $\Delta\bar{a}$ peaks of both MBs towards lower excitation frequencies. The high-frequency peak of bubble A almost vanishes.

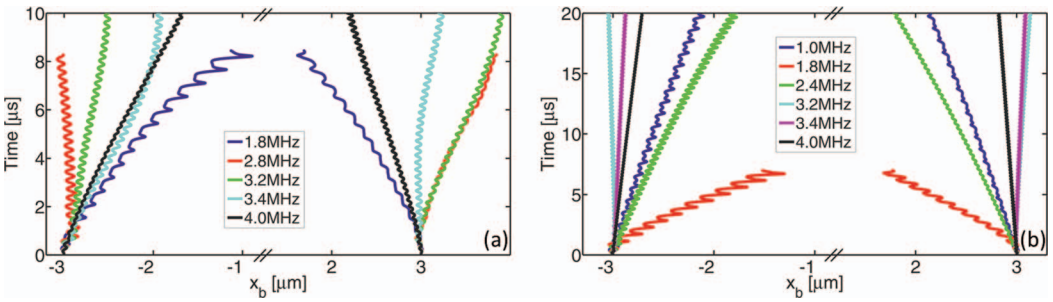


FIG. 9. Traces of the transient positions of MB centers with $d_{bb} = 6\ \mu$m inside a large liquid envelope exposed to $P_{ex} = 50$ kPa (setup II) (a) and inside a rigid tube of $r_t = 7.5\ \mu$m exposed to $P_{ex} = 40$ kPa (setup IV) (b) at various excitation frequencies. In setup II, the MBs transit from attraction at low $f_{ex}$ to repulsion in the intermediate range and back to attraction at high $f_{ex}$ values. Non-symmetric attraction at 1.8 MHz and 4.0 MHz and non-symmetric repulsion at 2.8 MHz is visible together with collective drift at 3.2 MHz and a change in motion direction at 3.4 MHz. For setup IV, non-symmetric phenomena are less pronounced and velocities are lower, but we identify non-symmetric attraction at 4.0 MHz, non-symmetric repulsion at 3.2 MHz, and collective drift at 3.4 MHz.

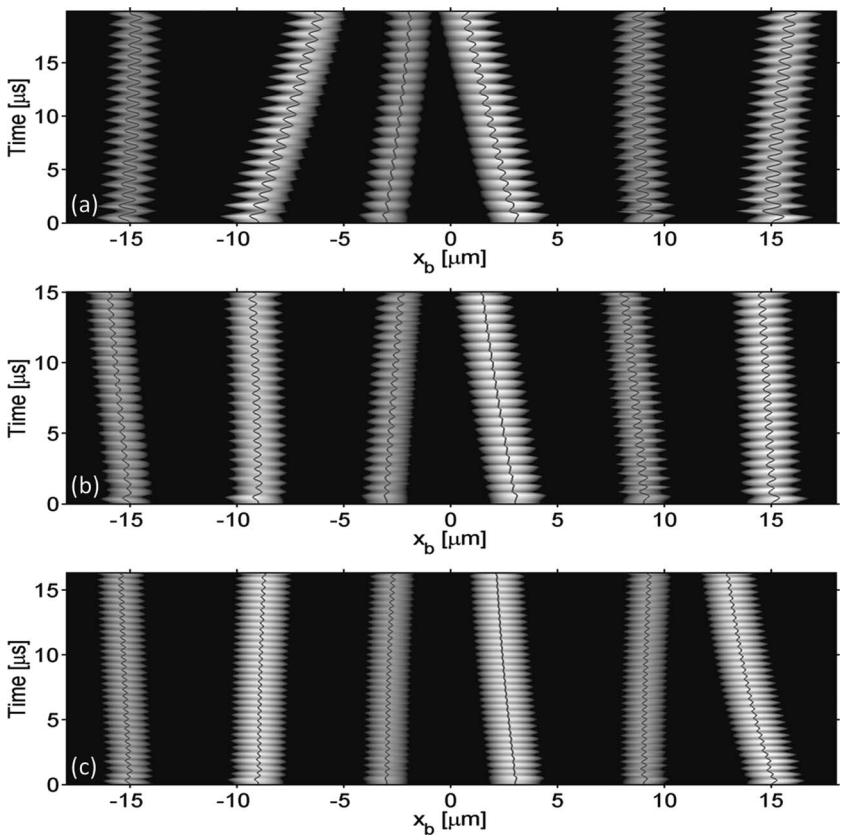


FIG. 10. Streak plots showing the vibrations and translatory motion of six interacting MBs in a narrow rigid tube of $r_t = 3\ \mu$m at $P_{ex} = 65$ kPa. (a) At $f_{ex} = 1$ MHz the innermost MBs attract each other, dragging the MB to their left with them, while the rightmost MB drifts away from the others. When increasing $f_{ex}$ to 1.5 MHz (b) and 2 MHz (c), the central attraction slows down, leaving the left neighboring MB in a static position and the rightmost MB is dragged inward.

translation in setup IV from moderate attraction at 1.0 MHz to strong attraction at 1.8 MHz and via moderate attraction at 2.4 MHz to asymmetric repulsion at 3.2 MHz. This is followed by collective drift at 3.4 MHz and again weak attraction at 4.0 MHz. A similar behavior involving larger velocities and more pronounced repulsion is found for setup II.

### D. Multi bubble systems

The computational framework used in this study is capable of handling an arbitrary number of bubbles. As an example, we illustrate a case of 6 MBs lined up along the axis of a narrow tube of $r_t = 3\ \mu$m, with initial bubble spacing of $d_{bb} = 6\ \mu$m. The MBs are alternatingly of size $a_{0,2m\text{-}1} = 1\ \mu$m and $a_{0,2m} = 1.2\ \mu$m, where $m$ is the index designating a MB. Figure 10 displays streak plots of those interacting MBs when exposed to a pressure field of $P_{ex} = 65$ kPa and $f_{ex}$ values of 1.0 MHz, 1.5 MHz, and 2.0 MHz, respectively. The interaction and the resulting translation behavior are expectedly more complex than in the setups with two bubbles: At 1.0 MHz, the innermost MBs attract each other and drag their left neighbor with them, while the rightmost bubble is slightly displaced away from the scene. With increasing $f_{ex}$, the speed of attraction between the innermost MBs weakens, their left neighbor remains in place and the rightmost MB changes direction and is dragged inward.

## IV. DISCUSSION

The results presented above document the dependence of $v_{bb}$ on insonation frequency, pressure amplitude, and confinement inside rigid tubes. They further illustrate changes in $\Delta\bar{a}_{max}$ and a shift

of $f_{\Delta\bar{a},max}$ when reducing $d_{bb}$, as well as changes in $\theta$ and $\Delta\bar{a}$ in confinement and upon variation of $P_{ex}$. Using streak plot visualization, non-symmetric translation phenomena and reversal of motion direction were identified. Finally, the dynamics of a more complex setup of six confined MBs was investigated, demonstrating the ability of the presented computational framework to model the interaction of multiple, closely spaced and confined MBs. Such intricate configurations are not accessible to full-scale theoretical investigations and have, to our knowledge, not been investigated numerically before.

In addition to verifying the numerical accuracy of our modeling approach, we confirmed that the transient simulations are able to reproduce the physical patterns predicted by theory[11] with good long-term stability and reliability (see Appendices A and B). Moreover, the $f_{\Delta\bar{a},max}$ values for setup I (Figure 2) correspond closely to the predicted values for individual MBs, as expected for large $d_{bb}$, where the MB dynamics should be basically decoupled. For low $P_{ex}$, the prediction was based on an analytical relation (6) while in the non-linear regime theoretical values are derived from the RPE. The deviations of the $\Delta\bar{a}$ pattern of the smaller bubble A from the predictions is assigned to the long-range influence of the larger bubble B, which itself exhibits a frequency response in close accordance with predictions.

A comparison between our modeling approach and the force balance approach (see Appendix B) often employed for theoretical studies yields good qualitative agreement for non-confined MBs. The analytical approaches are based on several simplifications, assumptions and empirical coefficients that may vary in the course of an oscillation cycle. In contrast, the present computational approach employs the complete conservation principles as described earlier, making it more generally applicable to arbitrary setups.

The excitation pressure amplitude has a marked effect on the $\Delta\bar{a}$ response (Figure 2) and the translatory behavior (Figure 5) of a pair of dissimilar MBs. The low frequency slopes of the peaks in the frequency response steepen with increasing $P_{ex}$ in accordance with findings by Lauterborn[13] and part of the excitation energy is transferred to subharmonics,[66] resulting in secondary low frequency peaks. A decrease of resonance frequency for widely spaced MBs with growing $P_{ex}$ is observed in agreement with literature predictions for single bubbles with clean interface.[13,67] The developed CF allows for going beyond the single MB configuration, revealing a splitting of the resonance peak of bubble A into a high and a low frequency segment (Figure 4) due to the influence of a larger neighboring MB. This pattern shifts towards lower frequencies with increasing $P_{ex}$ with a constant frequency gap.

When MBs move closer to each other, their resonance properties change due to the coupling to their neighbor.[28,68] This effect is visible in Figure 3, which also indicates that the dynamics of the larger MB change considerably less than those of the smaller MB.[69] The larger MB perceives the smaller partner as a mere particle entrained in its oscillatory near field flow and is not significantly disturbed by the small bubble's vibrations. Conversely, the forced pulsatile translation of the smaller MB due to the vibration of the bigger MB imposes the frequency characteristics of the larger onto the smaller bubble, leading to the alignment of their $f_{\Delta\bar{a},max}$.

This alignment promotes a strong attractive behavior in the $v_{bb}$ pattern around the common $f_{\Delta\bar{a},max}$. The $f_{ex}$ range of MB repulsion widens with increasing $P_{ex}$ (Figure 5) and the repulsive velocities become comparable in magnitude to the attractive velocities. The transition between repulsion and attraction is marked by the phase shift $\theta$ surpassing 90°, as predicted by theory.[17] Together with the $\Delta\bar{a}$ pattern, the $v_{bb}$ response and the $\theta$ distribution shift towards lower $f_{ex}$ with increasing $P_{ex}$.

In confinement, the resonance frequencies ($f_r$) of the MBs are expected to decrease with decreasing $r_t$[12] due to the inertia of the liquid column and viscous damping at the walls. This is reflected in the shift of $\Delta\bar{a}$ patterns towards lower frequencies and the shrinking of the high-frequency peak of the smaller bubble (Figure 8). This effect is accompanied by a change in $v_{bb}$ patterns, where the repulsion domain and the high frequency attraction are diminished compared to low frequency attraction. This occurs due to the establishment of small $\Delta\bar{a}$ in the high $f_{ex}$ range, leading to reduced liquid agitation and an increase of $\Delta\bar{a}$ at low $f_{ex}$. Furthermore, the decrease in magnitude of $v_{bb}$ in narrower tubes correlates with reduced $\Delta\bar{a}_{max}$ values. The decrease of $f_r$ in confinement causes a change in the phase relation between an individual MB and the external excitation, which in turn

alters the mutual MB phase shift $\theta$. We observe a translation of the main $\theta$ peak towards lower $f_{ex}$ values in confinement. In accordance with the identified correlation between the change of sign in $v_{bb}$ and $\theta$ crossing 90°, the $v_{bb}$ pattern equally shifts towards lower frequencies.

Cases of non-symmetric translation upon attraction or repulsion of two non-equal MBs or collective drift were identified in our results (Figures 6 and 9). These phenomena are attributed to differences in drag and inertia of the MBs and do not contradict momentum conservation due to the viscous nature of the liquid. Non-symmetric translation of two differently sized MBs is predicted by Oguz and Prosperetti[19] and, according to Doinikov,[21] the symmetry in forces and thus in motion of the two bubbles will be broken by the dissipative processes in a viscous host liquid. Hence, the bubble system may attain a non-zero linear momentum and even motion of both MBs in the same direction can occur.[20] In some cases we observed inversion of the motion from attraction to repulsion. The growing coupling of the approaching MBs influences their resonance properties, leading to an increase of $\theta$ and eventually an inversion of transverse motion. Such phenomena have been experimentally observed by Yoshida *et al.*[30] and theoretically predicted by Ida.[22] To our knowledge, the present computational model is the first to reproduce these phenomena.

The numerical approach provides access to all relevant kinematic and dynamic quantities such as $V_b$, $\bar{a}$, $\mathbf{x}_\mathrm{b}$, instantaneous shape of each bubble, $P_b$, $d_{bb}$, $v_{bb}$, oscillation phase relative to the excitation, $\theta$, and fluid forces. In advancing the state of the art compared to analytical models valid for special cases, our computational model brings with it significant generality and allows the study of multiple MBs of different sizes in close proximity and in arbitrary configurations including confinement. The modeling of linear and non-linear oscillations as well as translatory phenomena is within the scope of the CF. Starting from an undisturbed system, the transient simulation can provide insight into the initial transition phase. While this work concentrates on rather small MBs of around 1 $\mu$m equilibrium radius as appropriate for medical applications, there is no restriction to the application of the developed computational framework to setups of larger bubbles.

## V. CONCLUSIONS

The purpose of this study was twofold: to introduce, verify, and establish a novel computational method based on FVM and interface tracking for modeling multiple interacting MBs in a viscous host liquid, and to employ this method to investigate the impact of proximity, excitation amplitude, and spatial confinement on interacting MBs, focusing on their translatory motion. We studied setups with pairs of dissimilar MBs at variable distance and inside rigid tubes of variable radius. Those were exposed to transient excitation pressure of variable amplitude and frequency to highlight the versatility and generality of the presented CF. Non-linear characteristics such as steepening of low frequency slopes, secondary peaks and non-spherical MB shapes are observed for increased pressure levels, where the frequency domain of repulsion widens and becomes more prominent. In confinement, the repulsive motion weakens relative to attraction and the translation velocity peaks shift to lower frequencies along with the amplitude maxima of the two MBs. A correlation between the onset of repulsion and the vibration phase offset surpassing 90° was found. Phenomena like non-symmetrical relative motion, collective drift or inversion of motion direction were identified in MB translation. Pairs of similar MBs consistently exhibited attraction in accordance to theoretical predictions. The ability to treat arrangements of multiple bubbles was illustrated for a configuration hosting six MBs.

## ACKNOWLEDGMENTS

The authors would like to thank Dr. M. K. Tiwari, Dr. F. Rikhtegar, Ch. Sharma, B. Siyahhan, and B. Grieser for their valuable comments and advice. We gratefully acknowledge the funding of this research by the Swiss National Science Foundation through the NCCRs Co-Me and Kidney.CH.

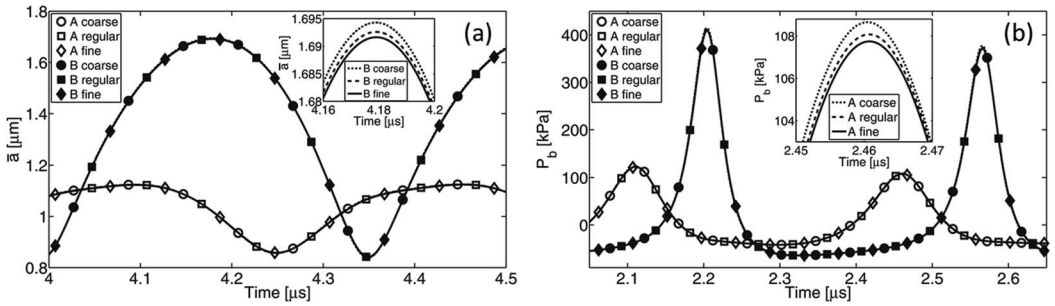


FIG. 11. Temporal development of average bubble radius (a) and average fluid pressure at the bubble surface (b) for both bubbles A and B on three successively refined grids. The overall pattern agreement for all considered mesh configurations was excellent, with the largest deviations located around the extrema of the radius and the maxima of pressure. The insets (on a significantly enlarged scale to make the differences visible) show these regions in detail and suggest a gradual decrease in difference between the solutions with refinement.

## APPENDIX A: COMPUTATIONAL ACCURACY

Here we assess the numerical validity of our results by varying the refinement of the computational grid as well as the time step size ($\Delta t$) of the transient calculation and show the independence of the converged solution from those variations.

### 1. Grid independence

A configuration comprising two MBs of equilibrium radii $a_{0,A} = 1.0\ \mu$m and $a_{0,B} = 1.2\ \mu$m at a distance $d_{AB} = 6\ \mu$m inside a large spherical liquid envelop of $R_L = 100\ \mu$m excited by a transient sinusoidally varying pressure of amplitude $P_{ex} = 50$ kPa and frequency $f_{ex} = 2.8$ MHz was selected as the reference case. Three similarly structured meshes comprising 39 808 cells, 76 200 cells, and 129 888 cells, respectively (resulting from consecutive decreases of the edge length of the computational cells by 20%), were created for this geometry. These mesh configurations are accordingly referred to as coarse (index $c$), regular (index $r$), and fine (index $f$). The converged solutions on those three meshes are compared with respect to parameters such as the average bubble radius ($\bar{a}$) and the average fluid pressure at the bubble surface ($P_b$) as shown in Figure 11.

The acquired solutions for the three grid refinement levels show a very good agreement with the largest deviations situated around the extrema of the respective graphs. A closer inspection reveals that the small difference between the results decreases with growing refinement. We further quantify the impact of mesh refinement by the relative change in individual parameters, such as bubble volume $V_b$, $\bar{a}$, or $P_b$, at a specific sampling time defined as

$$\varepsilon(t) = \left| \frac{s_1(t) - s_2(t)}{s_{2,\max} - s_{2,\min}} \right|, \tag{A1}$$

where $s_1$ is the transient parameter value on the respective coarser mesh and $s_2$ is its value on the finer mesh, while $s_{2,max}$ and $s_{2,min}$ denote the overall maximum and minimum on the finer mesh. For the investigated setup, the maximum relative errors in $\bar{a}$ comparing the coarse and regular grid were $\varepsilon_{cr,A}(\bar{a}) = 2.2\%$ for bubble A and $\varepsilon_{cr,B}(\bar{a}) = 0.3\%$ for bubble B. These reduce to $\varepsilon_{rf,A}(\bar{a}) = 0.55\%$ and $\varepsilon_{rf,B}(\bar{a}) = 0.19\%$ when comparing the regular and fine configurations. Similarly, the maximum relative errors in $V_b$ amount to $\varepsilon_{cr,A}(V_b) = 1.6\%$ and $\varepsilon_{cr,B}(V_b) = 0.44\%$ and reduce to $\varepsilon_{rf,A}(V_b) = 0.57\%$ and $\varepsilon_{rf,B}(V_b) = 0.21\%$. The maximum relative errors in $P_b$ decrease from $\varepsilon_{cr}(P_b) = 1.5\%$ for both bubbles to $\varepsilon_{rf,A}(P_b) = 1.0\%$ and $\varepsilon_{rf,B}(P_b) = 0.75\%$.

The monitored parameters show closely matching patterns and quantitative changes of 1% or less throughout the entire calculation time when comparing the regular to the fine mesh, which contains 70% more mesh cells. Considering a balance between precision and computational time requirements, the regular mesh is chosen as the ideal configuration and used further on. The other setups used in this study have been assessed accordingly and appropriate mesh settings were chosen.

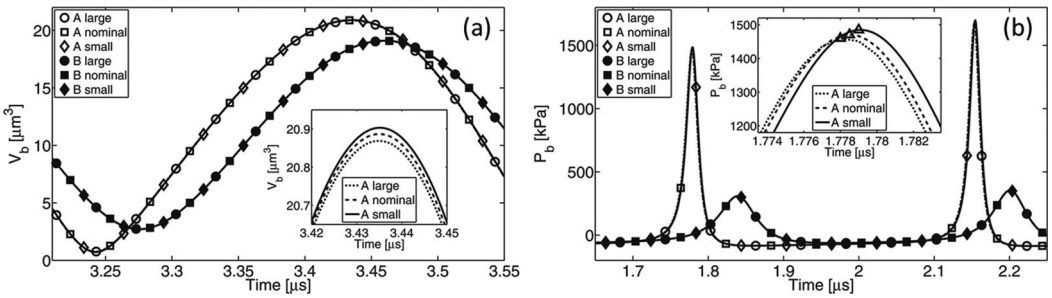


FIG. 12. Evolution of bubble volume (a) and average fluid pressure at the bubble surface (b) for both bubbles A and B using three consecutively shrinking time step settings. While the patterns match very well on a global scale, a detailed investigation shows minute temporal offsets between the three graphs, most notably at the sharp pressure peaks (shown in an expanded scale for visibility).

### 2. Time step independence

The influence of the choice of time step size ($\Delta t$) in this transient computation was assessed by comparing the solutions acquired from calculations on a single setup using three different time step values of $1 \times 10^{-9}$ s, $5 \times 10^{-10}$ s, and $2.5 \times 10^{-10}$ s, respectively, called large ($\Delta t_l$), nominal ($\Delta t_n$), and small ($\Delta t_s$) time step. A setup similar to the one used for the mesh independence assessment with the MBs separated by a distance of $d_{AB} = 40$ $\mu$m was examined. The variations of $V_b$ and $P_b$ (Figure 12) caused by a change of time step setting are considered as indicators for a proper choice of $\Delta t$.

Qualitatively the solutions for the three different time step settings agree very well and differences are only perceivable upon detailed inspection. They are largest in the peak regions and a minute temporal shift is noticeable when comparing the peaks of $P_b$. The quantitative comparison (A1) of the three configurations with respect to change of $V_b$ yields variations in the range of 0.8%–0.9% for both the comparisons between the solutions for $\Delta t_l$ and $\Delta t_n$ as well as $\Delta t_n$ and $\Delta t_s$ for bubble A and relative errors below 0.15% for the comparisons with respect to bubble B. A closer inspection of the results shows that eventually the converged solution for $\Delta t_n$ is closer to the solution for $\Delta t_l$ and on other occasions it is very close to the solution for $\Delta t_s$, while all three solutions stay within 1.3% of each other throughout the entire computation.

The main source of error regarding $P_b$ is a slight temporal offset between the solutions. This effect combined with the very rapid change of $P_b$ in time near the peaks makes the error determined by a comparison at every time instance appear unjustly high. Hence a comparison of the height of the individual peaks is preferred, as it offers a more balanced assessment. We define the relative change in peak height caused by a change in time step setting as

$$\varepsilon_{PP}(i) = \left| \frac{s_1(i) - s_2(i)}{s_{2,\max} - s_{2,\min}} \right|, \tag{A2}$$

where $i$ is the index of a peak. This metric yields maximum relative error values of 0.6%–0.8% for bubble A and around 0.1% for bubble B. Again no appreciable difference is observed when comparing the solutions for $\Delta t_l$ and $\Delta t_n$ or $\Delta t_n$ and $\Delta t_s$.

Based on the findings presented in this section, the value $\Delta t_n = 5 \times 10^{-10}$ s, which provides 2000 sampling points within the wavelength of a 1 MHz signal, was chosen.

## APPENDIX B: MODEL VERIFICATION

### 1. Single bubble model

To verify our computational model, we compare results obtained therewith to those of the RPE:[11]

$$\rho_L \left( a\ddot{a} + \frac{3}{2}\dot{a}^2 \right) = P_g - P_\infty - \frac{2\sigma}{a} - \frac{4\mu_L \dot{a}}{a}. \tag{B1}$$

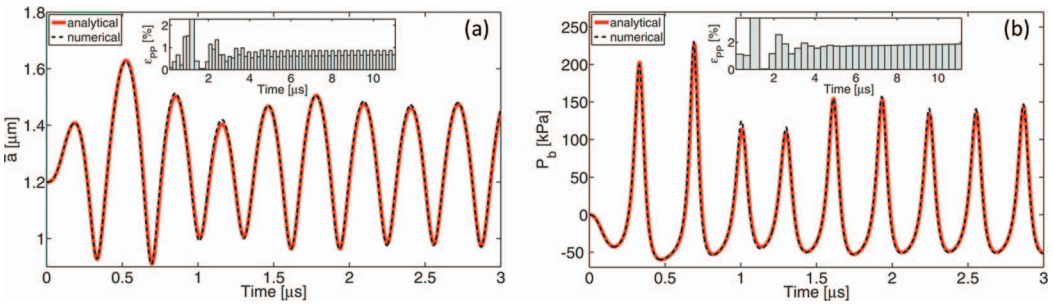


FIG. 13. Comparison between the numerical results and analytical predictions of the transient radius (a) and $P_b$ pattern (b) for a single MB excited by a time-varying pressure of $f_{ex} = 3.2$ MHz and $P_{ex} = 50$ kPa. The patterns match very well with discernible discrepancies only in the initial transition phase and around the extrema. The relative error in peak height for all extrema of the radius curve and for the maxima in pressure is shown in the respective insets.

Here, $a$ is the bubble radius, the dots denote derivation with respect to time, and $P_\infty$ is the liquid pressure at infinity.

The RPE model describes the oscillation of a single gas bubble in an infinite volume of liquid. While the requirement of an infinite liquid envelope is obviously not strictly implementable in grid-based numerical models, we chose to use a liquid sphere with $R_L = 100$ $\mu$m to host the bubble. To prove that this choice is sufficient to achieve an accurate solution for infinite surroundings, we compare the acquired results to the solution attained with a setup using a substantially larger liquid sphere of $R_L = 1000$ $\mu$m.

We quantify the impact of enlarging the setup by the relative change (A1) in a transient parameter such as bubble volume $V_b$ or average bubble radius $\bar{a}$, at a specific sampling time. We find that the choice of a larger liquid sphere causes a maximum relative error of close to 3% in the temporal development of the average radius $\bar{a}$ of two MBs of $a_{0,A} = 1.0$ $\mu$m and $a_{0,B} = 1.2$ $\mu$m separated by a distance $d_{AB} = 6$ $\mu$m and exposed to an oscillating pressure field of $f_{ex} = 2.8$ MHz and $P_{ex} = 50$ kPa. Relative to a tenfold increase in radius of the liquid sphere, this error is clearly acceptable taking into account the computational time constraints imposed by a large extension of the mesh size.

To verify the employed numerical solver we chose a configuration with a single bubble of equilibrium radius $a_0 = 1.2$ $\mu$m excited by pressure oscillations of amplitude $P_{ex} = 50$ kPa and frequencies of 2.8 MHz or 3.2 MHz. Figure 13 shows a comparison for the MB radius and the pressure at the bubble interface $P_b$ between the results acquired from numerical simulations and the predictions from (B1). The match between the patterns is very good and even improves after an initial transition phase. The maximum relative errors (A1) in bubble radii are 6.3% and 4.2% for the respective frequencies. After an initial transitional phase of 3 $\mu$s these errors level off to below 1.6% and 2%, respectively.

The main cause of the error is a small temporal offset between the numerical and the analytical solution. Therefore we deem a comparison of peak height values (A2) more appropriate. For the radius comparison in both investigated cases we find $\varepsilon_{pp} = 2.3\%$, which reduces to below 1% after the first 3 $\mu$s. For $P_b$, the analysis yields $\varepsilon_{pp} = 4.3\%$ for a 2.8 MHz excitation which reduces to 2.3% after the initial 3 $\mu$s, and $\varepsilon_{pp} = 3.8\%$ for 3.2 MHz, reducing to 1.9% after the initial 3 $\mu$s. This excellent agreement between the numerical results and the analytically predicted patterns is achieved with a mesh comprising 78 200 computational cells. This is similar in resolution to the regular setup described in Appendix A, Subsection 1.

To confirm the incompressibility assumption for the liquid, we compared the oscillation patterns predicted by the RPE with those obtained using the Keller-Miksis equation[10] for the $f_{ex}$ and $P_{ex}$ ranges relevant in this study. The relative differences between the radius predictions of the two models normalized by the maximum oscillation range $\Delta a_{max}$ were assessed for MBs of $a_0 = 1.0$ $\mu$m and $a_0 = 1.2$ $\mu$m, and were found to be below 3% except for two sets of $f_{ex}$ and $P_{ex}$ values where they reached up to 8%. The parameter settings yielding the highest relative errors coincide with the $\Delta a$ peaks of the RPE solution in Figure 2 (grey lines).

### 2. Comparison to force balance model

Theoretical descriptions of the interaction of two bubbles usually focus on identifying the acting forces and working out a force balance.[29,30] The main acting forces on bubbles driven by a transient but spatially homogeneous ultrasound field are identified as the secondary Bjerknes force $\mathbf{f}_{B2}$, the viscous drag force $\mathbf{f}_d$, and the added mass force $\mathbf{f}_a$, where $\mathbf{f}_{B2} + \mathbf{f}_d + \mathbf{f}_a = 0$. $\mathbf{f}_{B2}$ may be written for two compressible gas cavities inside an incompressible liquid according to Mettin *et al.*[18] as

$$\mathbf{f}_{B2} = -V_B \nabla P = \frac{\rho}{4\pi d_{AB}^2} V_B \frac{d^2 V_A}{dt^2} \mathbf{e}_d \tag{B2}$$

with the unit vector $\mathbf{e}_d$ pointing along the axis connecting the bubble centers, and the indices A and B designating different bubbles. The drag exerted on the bubble, which results from translatory motion in a viscous medium, may be written as

$$\mathbf{f}_d = -6\pi\mu a \mathbf{v}_r \tag{B3}$$

for Reynolds numbers of the order unity. The velocity of the bubble relative to the fluid is denoted by $\mathbf{v}_r = \mathbf{v}_b - \mathbf{v}(\mathbf{x}_b)$, where $\mathbf{v}_b = \mathrm{d}(\mathbf{x}_b)/\mathrm{d}t$ is the absolute velocity of the bubble derived from the temporal change of the position $\mathbf{x}_b$ of its center of gravity and $\mathbf{v}(\mathbf{x}_b)$ is the absolute velocity of the fluid at the position of the bubble. This quantity is approximated by the speed of the flow created by the neighboring bubble at the position of the considered bubble

$$\mathbf{v}(\mathbf{x}_A) = \frac{a_B^2 \dot{a}_B}{d_{bb}^2} \mathbf{e}_d. \tag{B4}$$

This approach is approximately valid if the affected bubble is small compared to the distance $d_{bb}$ from its neighbor and if its own oscillations cause only minor disturbances to the flow field. Finally, the added mass force felt by the bubble can be written as

$$\mathbf{f}_a = -\frac{\rho}{2} \frac{d}{dt} (V_b \mathbf{v}_r). \tag{B5}$$

This expression contains a term $\mathrm{d}\mathbf{v}_b/\mathrm{d}t = \boldsymbol{\alpha}$ which represents the acceleration of the bubble. All these force expressions assume certain values for coefficients such as drag coefficient and the coefficient of added mass, which depend on the flow conditions and may change during an oscillation cycle. Further, the bubbles have to be considered as far away from each other, static and point-like objects in order to calculate $\mathbf{v}_r$ analytically.

In contrast, our numerical model is based on the direct application of the basic physical principles of mass conservation and momentum conservation without relying on any assumptions as to the shape of the bubbles, flow conditions or size of the added mass envelop. A comparison of the numerical with the analytical results is thus expected to yield only a qualitative agreement, with the numerical results giving a more accurate representation of reality.

The acceleration of the MBs in the numerical results is derived from the temporal development of the position of its center of gravity as $\boldsymbol{\alpha}_n = \ddot{\mathbf{x}}_b$, while the equivalent acceleration predicted by the analytical model is

$$\boldsymbol{\alpha} = \frac{d\mathbf{v}_b}{dt} = \frac{2(\mathbf{f}_{B2} + \mathbf{f}_d)}{\rho V_b} - \frac{\dot{V}_b}{V_b} \mathbf{v}_r(\mathbf{x}_b) + \dot{\mathbf{v}}(\mathbf{x}_b). \tag{B6}$$

Here the instantaneous bubble volumes, average radii, radial and translational velocities are supplied by the numerical simulation. Figure 14 shows the comparison between the analytical model and our numerical results with respect to bubble acceleration for a pair of MBs that are 40 $\mu$m apart and two closely spaced MBs with $d_{AB} = 6$ $\mu$m, both pairs being excited by a 2.8 MHz transient pressure field with $P_{ex} = 50$ kPa.

The general patterns agree for both comparisons, while locally notable deviations become apparent. We observe differences in the maximum values and the appearance of an additional shoulder in the analytical results for the larger bubble B. According to our assessment, the height of the analytically predicted peaks depends on the choice of the added mass coefficient and drag

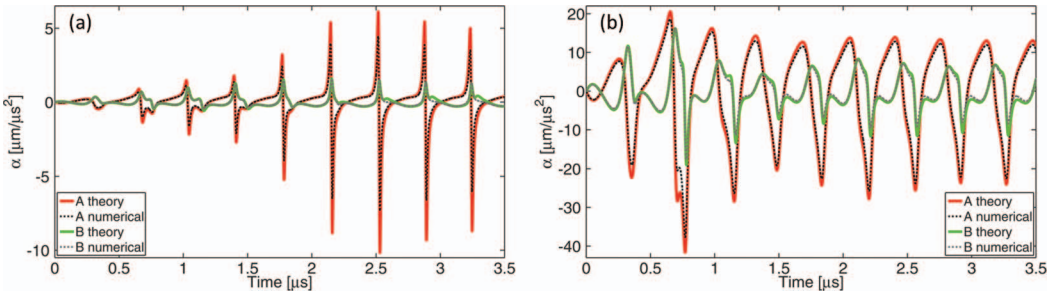


FIG. 14. Comparison of the predicted acceleration from the analytical model based on a force balance and the numerical results for a pair of MBs positioned 40 $\mu$m apart (a) and a pair of MBs spaced at 6 $\mu$m (b) in a 2.8 MHz ultrasound field at $P_{ex} = 50$ kPa. A close qualitative agreement between the patterns is observable together with reduced numerical peak values and the appearance of additional shoulders in the analytical prediction for bubble B.

coefficient and the appearance of the additional shoulder in those plots scales with the absolute liquid velocity.

We stress that this comparison should be seen in the light that the derivations of the above forces and of $\mathbf{v}_r$ are based on various simplifications or assumptions. Several coefficients need to be chosen according to parameter models and those coefficients, like the drag coefficient, may vary in the course of an oscillation cycle. Hence, quantitative differences seen in Figure 14 point to inherent shortcomings of the analytical model rather than to inaccuracies of the numerical simulation.

[1] T. J. Bulat, "Macrosonics in Industry: 3. Ultrasonic Cleaning," Ultrasonics **12**(2), 59–68 (1974).
[2] G. W. Gale and A. A. Busnaina, "Removal of particulate contaminants using ultrasonics and megasonics: A review," Particul. Sci. Technol. **13**(3–4), 197–211 (1995).
[3] L. Jatzwauk, H. Schone, and H. Pietsch, "How to improve instrument disinfection by ultrasound," J. Hosp. Infect. **48**, S80–S83 (2001).
[4] T. Nishikawa, A. Yoshida, A. Khanal, M. Habu, I. Yoshioka, K. Toyoshima, T. Takehara, T. Nishihara, K. Tachibana, and K. Tominaga, "A study of the efficacy of ultrasonic waves in removing biofilms," Gerodontology **27**(3), 199–206 (2010).
[5] E. Stride and N. Saffari, "Microbubble ultrasound contrast agents: A review," P I Mech. Eng. H **217**(H6), 429–447 (2003).
[6] K. Ferrara, R. Pollard, and M. Borden, "Ultrasound microbubble contrast agents: Fundamentals and application to gene and drug delivery," Annu. Rev. Biomed. Eng. **9**, 415–447 (2007).
[7] K. Hynynen, N. McDannold, N. A. Sheikov, F. A. Jolesz, and N. Vykhodtseva, "Local and reversible blood-brain barrier disruption by noninvasive focused ultrasound at frequencies suitable for trans-skull sonications," Neuroimage **24**(1), 12–20 (2005).
[8] N. McDannold, N. Vykhodtseva, and K. Hynynen, "Targeted disruption of the blood-brain barrier with focused ultrasound: Association with cavitation activity," Phys. Med. Biol. **51**(4), 793–807 (2006).
[9] W. Wiedemair, Z. Tukovic, H. Jasak, D. Poulikakos, and V. Kurtcuoglu, "On ultrasound-induced microbubble oscillation in a capillary blood vessel and its implications for the blood-brain barrier," Phys. Med. Biol. **57**(4), 1019–1045 (2012).
[10] A. Prosperetti, "Acoustic cavitation series. 2. Bubble phenomena in sound fields. 1," Ultrasonics **22**(2), 69–78 (1984).
[11] M. S. Plesset and A. Prosperetti, "Bubble dynamics and cavitation," Annu. Rev. Fluid Mech. **9**, 145–185 (1977).
[12] H. N. Oguz and A. Prosperetti, "The natural frequency of oscillation of gas bubbles in tubes," J. Acoust. Soc. Am. **103**(6), 3301–3308 (1998).
[13] W. Lauterborn, "Numerical investigation of nonlinear oscillations of gas-bubbles in liquids," J. Acoust. Soc. Am. **59**(2), 283–293 (1976).
[14] N. de Jong, P. J. Frinking, A. Bouakaz, M. Goorden, T. Schourmans, X. Jingping, and F. Mastik, "Optical imaging of contrast agent microbubbles in an ultrasound field with a 100-MHz camera," Ultrasound Med. Biol. **26**(3), 487–492 (2000).
[15] C. T. Chin, C. Lancee, J. Borsboom, F. Mastik, M. E. Frijlink, N. de Jong, M. Versluis, and D. Lohse, "Brandaris 128: A digital 25 million frames per second camera with 128 highly sensitive frames," Rev. Sci. Instrum. **74**(12), 5026–5034 (2003).
[16] V. Bjerknes, "Research on the hydrodynamic force field," Acta Math. **30**(2), 99–143 (1906).
[17] L. A. Crum, "Bjerknes forces on bubbles in a stationary sound field," J. Acoust. Soc. Am. **57**(6), 1363–1370 (1975).
[18] R. Mettin, I. Akhatov, U. Parlitz, C. D. Ohl, and W. Lauterborn, "Bjerknes forces between small cavitation bubbles in a strong acoustic held," Phys. Rev. E **56**(3), 2924–2931 (1997).
[19] H. N. Oguz and A. Prosperetti, "A generalization of the impulse and virial theorems with an application to bubble oscillations," J. Fluid Mech. **218**, 143–162 (1990).
[20] N. A. Pelekasis, A. Gaki, A. Doinikov, and J. A. Tsamopoulos, "Secondary Bjerknes forces between two bubbles and the phenomenon of acoustic streamers," J. Fluid Mech. **500**, 313–347 (2004).
[21] A. A. Doinikov, "Bjerknes forces between two bubbles in a viscous fluid," J. Acoust. Soc. Am. **106**(6), 3305–3312 (1999).
[22] M. Ida, "A characteristic frequency of two mutually interacting gas bubbles in an acoustic field," Phys. Lett. A **297**(3–4), 210–217 (2002).

[23] N. A. Pelekasis and J. A. Tsamopoulos, "Bjerknes forces between 2 bubbles. 2. Response to an oscillatory pressure field," J. Fluid Mech. **254**, 501–527 (1993).
[24] A. Harkin, T. J. Kaper, and A. Nadim, "Coupled pulsation and translation of two gas bubbles in a liquid," J. Fluid Mech. **445**, 377–411 (2001).
[25] A. A. Doinikov, "Acoustic radiation interparticle forces in a compressible fluid," J. Fluid Mech. **444**, 1–21 (2001).
[26] A. A. Doinikov and S. T. Zavtrak, "On the mutual interaction of two gas bubbles in a sound field," Phys. Fluids **7**(8), 1923–1930 (1995).
[27] A. A. Doinikov, *Bubble and Particle Dynamics in Acoustic Fields: Modern Trends and Applications* (Research Signpost, 2005).
[28] V. Garbin, D. Cojoc, E. Ferrari, E. Di Fabrizio, M. L. J. Overvelde, S. M. van der Meer, N. de Jong, D. Lohse, and M. Versluis, "Changes in microbubble dynamics near a boundary revealed by combined optical micromanipulation and high-speed imaging," Appl. Phys. Lett. **90**(11), 114103 (2007).
[29] P. Marmottant, M. Versluis, N. de Jong, S. Hilgenfeldt, and D. Lohse, "High-speed imaging of an ultrasound-driven bubble in contact with a wall: "Narcissus" effect and resolved acoustic streaming," Exp. Fluids **41**(2), 147–153 (2006).
[30] K. Yoshida, T. Fujikawa, and Y. Watanabe, "Experimental investigation on reversal of secondary Bjerknes force between two bubbles in ultrasonic standing wave," J. Acoust. Soc. Am. **130**(1), 135–144 (2011).
[31] P. L. Marston, E. H. Trinh, J. Depew, and T. J. Asaki, "Response of bubbles to ultrasonic radiation pressure: Dynamics in low gravity and shape oscillations," Fluid Mec. A **23**, 343–353 (1994).
[32] A. A. Doinikov and S. T. Zavtrak, "On the "bubble grapes" induced by a sound field," J. Acoust. Soc. Am. **99**(6), 3849–3850 (1996).
[33] C. W. Hirt and B. D. Nichols, "Volume of fluid (Vof) method for the dynamics of free boundaries," J. Comput. Phys. **39**(1), 201–225 (1981).
[34] S. Osher and J. A. Sethian, "Fronts propagating with curvature-dependent speed: Algorithms based on Hamilton-Jacobi formulations," J. Comput. Phys. **79**(1), 12–49 (1988).
[35] I. L. Chern, J. Glimm, O. Mcbryan, B. Plohr, and S. Yaniv, "Front tracking for gas-dynamics," J. Comput. Phys. **62**(1), 83–110 (1986).
[36] S. O. Unverdi and G. Tryggvason, "A front-tracking method for viscous, incompressible, multi-fluid flows," J. Comput. Phys. **100**(1), 25–37 (1992).
[37] M. V. Annaland, N. G. Deen, and J. A. M. Kuipers, "Numerical simulation of gas bubbles behaviour using a three-dimensional volume of fluid method," Chem. Eng. Sci. **60**(11), 2999–3011 (2005).
[38] M. V. Annaland, W. Dijkhuizen, N. G. Deen, and J. A. M. Kuipers, "Numerical simulation of behavior of gas bubbles using a 3-D front-tracking method," AICHE J. **52**(1), 99–110 (2006).
[39] A. Tomiyama, S. Takagi, and Y. Matsumoto, "Numerical simulation of bubble flows using interface tracking and bubble tracking methods," Comput. Exp. Meth. **1**, 191–206 (1999).
[40] D. Gueyffier, J. Li, A. Nadim, R. Scardovelli, and S. Zaleski, "Volume-of-fluid interface tracking with smoothed surface stress methods for three-dimensional flows," J. Comput. Phys. **152**(2), 423–456 (1999).
[41] K. L. Pan and Z. J. Chen, "Simulation of bubble dynamics in a microchannel using a front-tracking method," Comput. Math. Appl. **67**(2), 290–306 (2014).
[42] T. Ye, W. Shyy, and J. N. Chung, "A fixed-grid, sharp-interface method for bubble dynamics and phase change," J. Comput. Phys. **174**(2), 781–815 (2001).
[43] T. Ye and J. L. Bull, "Microbubble expansion in a flexible tube," J. Biomech. Eng.-T Asme **128**(4), 554–563 (2006).
[44] N. Hosseinkhah and K. Hynynen, "A three-dimensional model of an ultrasound contrast agent gas bubble and its mechanical effects on microvessels," Phys. Med. Biol. **57**(3), 785–808 (2012).
[45] A. M. Zhang, X. L. Yao, and L. H. Feng, "The dynamic behavior of a gas bubble near a wall," Ocean Eng. **36**(3–4), 295–305 (2009).
[46] C.-T. Hsiao and G. L. Chahine, "Numerical modeling of non-spherical response of therapeutic encapsulated microbubbles to ultrasound," AIP Conf. Proc. **1359**(1), 443–448 (2011).
[47] N. Mendez and R. Gonzalez-Cinca, "Numerical study of bubble dynamics with the boundary element method," J. Phys. Conf. Ser. **327**, 012028 (2011).
[48] T. Kawamura and Y. Kodama, "Numerical simulation method to resolve interactions between bubbles and turbulence," Int. J. Heat Fluid **23**(5), 627–638 (2002).
[49] H. G. Weller, G. Tabor, H. Jasak, and C. Fureby, "A tensorial approach to computational continuum mechanics using object-oriented techniques," Comput. Phys. **12**(6), 620–631 (1998).
[50] Z. Tukovic and H. Jasak, "A moving mesh finite volume interface tracking method for surface tension dominated interfacial fluid flow," Comput. Fluids **55**, 70–84 (2012).
[51] T. Szabo, *Diagnostic Ultrasound Imaging: Inside Out* (Academic Press, 2004).
[52] H. Jasak and Z. Tukovic, "Automatic mesh motion for the unstructured finite volume method," Trans. Famena **30**(2), 1–18 (2007).
[53] I. Demirdzic and M. Peric, "Space conservation law in finite volume calculations of fluid-flow," Int. J. Numer. Meth. **8**(9), 1037–1050 (1988).
[54] D. Phillips, X. C. Chen, R. Baggs, D. Rubens, M. Violante, and K. J. Parker, "Acoustic backscatter properties of the particle/bubble ultrasound contrast agent," Ultrasonics **36**(8), 883–892 (1998).
[55] J. H. Ferziger and M. Peric, *Computational Methods for Fluid Dynamics* (Springer Verlag, Berlin, 1995).
[56] R. I. Issa, "Solution of the implicitly discretized fluid-flow equations by operator-splitting," J. Comput. Phys. **62**(1), 40–65 (1986).
[57] J. Zhang, D. M. Eckmann, and P. S. Ayyaswamy, "A front tracking method for a deformable intravascular bubble in a tube with soluble surfactant transport," J. Comput. Phys. **214**(1), 366–396 (2006).

[58] M. O. Culjat, D. Goldenberg, P. Tewari, and R. S. Singh, "A review of tissue substitutes for ultrasound imaging," Ultrasound Med. Biol. **36**(6), 861–873 (2010).
[59] J. M. Gorce, M. Arditi, and M. Schneider, "Influence of bubble size distribution on the echogenicity of ultrasound contrast agents: A study of SonoVue (TM)," Invest. Radiol. **35**(11), 661–671 (2000).
[60] D. E. Goertz, N. de Jong, and A. F. W. van der Steen, "Attenuation and size distribution measurements of definity (TM) and manipulated definity (TM) populations," Ultrasound Med. Biol. **33**(9), 1376–1388 (2007).
[61] T. Faez, D. Goertz, and N. De Jong, "Characterization of definity (Tm) ultrasound contrast agent at frequency range of 5-15 Mhz," Ultrasound Med. Biol. **37**(2), 338–342 (2011).
[62] M. Bertossi, D. Virgintino, E. Maiorano, M. Occhiogrosso, and L. Roncali, "Ultrastructural and morphometric investigation of human brain capillaries in normal and peritumoral tissues," Ultrastruct. Pathol. **21**(1), 41–49 (1997).
[63] D. B. Khismatullin, "Resonance frequency of microbubbles: Effect of viscosity," J. Acoust. Soc. Am. **116**(3), 1463–1473 (2004).
[64] H. R. Zheng, P. A. Dayton, C. Caskey, S. K. Zhao, S. P. Qin, and K. W. Ferrara, "Ultrasound-driven microbubble oscillation and translation within small phantom vessels," Ultrasound Med. Biol. **33**(12), 1978–1987 (2007).
[65] K. Tyml, D. Anderson, D. Lidington, and H. M. Ladak, "A new method for assessing arteriolar diameter and hemodynamic resistance using image analysis of vessel lumen," Am. J. Physiol-Heart C **284**(5), H1721–H1728 (2003).
[66] A. Prosperetti, "Nonlinear oscillations of gas-bubbles in liquids: Transient solutions and connection between subharmonic signal and cavitation," J. Acoust. Soc. Am. **57**(4), 810–821 (1975).
[67] A. A. Doinikov, J. F. Haac, and P. A. Dayton, "Resonance frequencies of lipid-shelled microbubbles in the regime of nonlinear oscillations," Ultrasonics **49**(2), 263–268 (2009).
[68] E. A. Zabolotskaya, "Interaction of gas-bubbles in a sound field," Sov. Phys. Acoust. **30**(5), 365–368 (1984).
[69] J. S. Allen, D. E. Kruse, P. A. Dayton, and K. W. Ferrara, "Effect of coupled oscillations on microbubble behavior," J. Acoust. Soc. Am. **114**(3), 1678–1690 (2003).